Available online at www.sciencedirect.com
SCIENCE DIRECT®
Journal of Sound and Vibration 279 (2005) 89–117
JOURNAL OF SOUND AND VIBRATION
www.elsevier.com/locate/jsvi

On the stability of stay cables under light wind and rain conditions

D. Burton, D.Q. Cao, R.W. Tucker*, C. Wang

Department of Physics, Lancaster University, Lancaster LA1 4YB, UK

Received 26 June 2003; accepted 27 October 2003

Abstract

This article studies the aerodynamic induced vibration of stay cables (in cable-stayed bridges) under the combined effect of light wind and rain in terms of a section model with a dynamic rivulet oscillating on a moving cable perimeter in a steady wind. The motion of the cable section is coupled with the motion of the rivulet via aerodynamic fluid–structure interactions. These complex interactions are modelled in two distinct ways and the resulting cable motions compared. The first employs an approximation that permits the use of data extrapolated from wind-tunnel measurements. The second approaches the aerodynamic interaction in terms of a sub-critical vortex description. In the first approach the stability of the linearized system is reduced to a six-dimensional eigenvalue problem and the dependence of the eigenvalues are explored numerically as a function of parameters that enter into the model. The predictions of the model rely on measured data for drag, lift and torque coefficients for fixed experimental cylinders with attached artificial rivulets, and data for the equilibrium location of rain-induced rivulets. In the second approach the dynamical evolution of the non-linear system of differential equations is explored and the results compared with those obtained in the first model. The results offer a useful means to understand how rain-wind induced vibrations of stay cables can arise and persist in terms of more realistic models than have been considered before in the literature.

1. Introduction

Long stay cables are important structural components of cable-stayed bridges. Due to their large flexibility and small structural damping, they are prone to vibration induced by motion of their supports and/or aerodynamic forces such as wind and rain loadings. Under the simultaneous occurrence of light-to-moderate wind and rain, large amplitude vibrations of stay cables have

*Corresponding author. Tel.: +44-0-1524-593610; fax: +44-0-1524-844037.
E-mail address: r.tucker@lancaster.ac.uk (R.W. Tucker).

0022-460X/$ - see front matter
doi:10.1016/j.jsv.2003.10.038

been observed in a number of cable-stayed bridges worldwide [1–4]. The mechanism leading to rain-wind induced vibration in stay cables has recently become of concern to bridge engineers and scientists in various countries, (see, for example, Refs. [5–11] and the references cited therein). Following the experimental investigations of Matsumoto et al. [6,9,12], aerodynamic instabilities of cables have been roughly divided into galloping motions and vortex-induced oscillations at reduced wind velocities U/fD between 40 and 80, where U is the wind speed, f (in Hz) a structural vibration frequency and D the diameter of the cable.

In a recent paper [11], a simple stochastic model that offers some insight into this mechanism has been constructed. Attention therein was drawn into the recent work that had been devoted to this problem [1,5,7,8,13] and its relation to earlier *galloping* mechanisms proposed by Den Hartog [14] and others [15–22]. It focused on the asymmetric cable section profile produced by the existence of a mobile rain rivulet on its surface and the corresponding induced aerodynamic forces. In that model the motion of the rivulet was assumed to be produced by a simple stochastic band-pass process that accommodated the steady state rivulet motion observed in static tests and led to a model exhibiting stochastic resonance. The steady stochastic response amplitude depended not only on aerodynamic coefficients and structural damping but also on certain filter parameters ω_f, ξ_f and S_0. Such parameters had to be determined from an effective power spectral density of the moving rivulet, measured from wind-rain tunnel tests and/or field measurements.

A more realistic approach would be to model the motion of the rivulet from the complex dynamics involving the boundary layers between the cable, rivulet and air. In this article a new, more physically motivated dynamic process is offered that couples the two-dimensional motion of a cable section to the motion of the rivulet. The model involves a complex fluid–structure interaction that is approximated in two distinct ways. The first employs an approximation that permits the use of data extrapolated from wind-tunnel measurements. The second approaches the aerodynamic interaction in terms of a sub-critical vortex description. In the first approach the stability of the linearized system is reduced to a six-dimensional eigenvalue problem and its eigenvalues are explored numerically as a function of parameters that enter into the model. The predictions of the model rely on measured data for drag, lift and torque coefficients for fixed experimental cylinders with attached artificial rivulets, and data for the equilibrium location of rain-induced rivulets. In the second approach the dynamical evolution of the non-linear system of differential equations is explored using an explicit vortex-tracking method and the results compared with those obtained in the first approximation. The results offer a useful means to understand how rain-wind induced vibrations of stay cables can arise and persist in terms of more realistic models than have been considered before in the literature. Although the *formation* of the rivulet by light rain will continue to require a stochastic element in a full description, this can in principle be included at the linear level along the lines given in [11].

Although intensive efforts have been made to investigate the phenomenon of rain-wind-induced vibrations of stay cables through wind tunnel tests, the analytical study of the growth mechanism of such a phenomenon is rare since the detailed motion of a cable with oscillating rivulets under wind forces is non-trivial. It involves the analysis of the equations of multi-phase fluid dynamics, a model for accretion and fluid–solid adhesion and the continuum mechanics of an elastic structure. Without detailed experimental information (or expensive time consuming computational fluid dynamic simulations) it is difficult to assess how rivulet formation on cylinders modifies the subsequent aerodynamic flow around them particularly when the cylinder moves relative to the

inflow fluid field [23]. However, in low ambient wind speeds, experiments with an artificial mobile rivulet on a fixed cylinder subject to aerodynamic loading do indicate an approach to a steady rivulet oscillation. In any mathematical model, once the profile of the rivulet is decided and its initial location on the cylinder ascertained one is confronted with the problem of estimating the aerodynamic forces and torque on an asymmetric structure. Wind tunnel tests on *fixed* cylinders for various *fixed* rivulet configurations and wind speeds offer data for *static configurations*, providing lift, drag and torque coefficients relative to the ambient wind tunnel velocity. In order to estimate these coefficients for a *moving* cylinder with a *mobile* rivulet relative to its circumference the simple strategy of using these coefficients in a certain co-moving frame derived from the dynamics of the moving cylinder section is adopted.

It is found that, after linearization, such an approximation leads to an eigenvalue problem that controls the onset of large amplitude vertical cable oscillations initiated by the oscillation of a single (upper) rivulet along the cable surface. Such a rivulet oscillation occurs only when the *effective* stiffness relating aerodynamic torque to the location of the rivulet on the cable surface, is positive. The use of wind-tunnel data for the aerodynamic drag, lift and torque coefficients on cylinders with various rivulets at fixed positions enables one to explore how the above eigenvalue spectrum of the system varies with parameters in the model. Time histories resulting from this linearized model for different values of various parameters are then calculated and discussed.

In order to go beyond the linearized level a more refined model of the fluid–structure interaction is deemed necessary. For sub-critical air flow in the vicinity of the cable (light wind) this can be attempted by a combination of simple boundary-layer modelling and a vortex description of boundary layer separation and subsequent convection of vorticity. Using analytic expressions for the fluid flow field due to a dynamic set of point vortices the pressure on a cable section is estimated due to the emission of such vortices. In this way one obtains a more reliable non-linear description of the dynamics of the moving cable in the presence moving rivulets. Such a model can then be solved numerically beyond the linear approximation considered in the first approach.

2. Model of a cable with a single rivulet

Consider first a spring-supported section model with a single artificial rivulet moving on its upper surface, as shown in Fig. 1. Although rivulets along both upper and lower cable surfaces have been observed in the case of rain-wind vibrations it is generally believed that the upper one is the dominant one in inducing cable vibration [1,5]. The cable, exposed to a steady wind of velocity $\mathbf{U}$ blowing from left to right, has a mass m per unit length and, in the section model, is supported by springs with coefficients k_x, k_y and dampers with damping coefficients c_x, c_y in the horizontal and vertical directions, respectively. The rivulet has a mass m_r per unit length and is bound to the cable surface by the combined actions of the wind, gravitational, friction and dynamic adhesive forces. In a section model the incoming steady wind is normal to the horizontal axis of the cylinder and the motion of the rivulet is independent of which section is taken. The transverse size of the rivulet is assumed to be small compared with the diameter of the cylinder.

Let $\{\mathbf{i}, \mathbf{j}, \mathbf{k}\}$ be the inertial frame with fixed origin as shown in Fig. 1. With A denoting the instantaneous centre of a cable section (restricted to the $\mathbf{i},\mathbf{j}$ plane) and B locating the

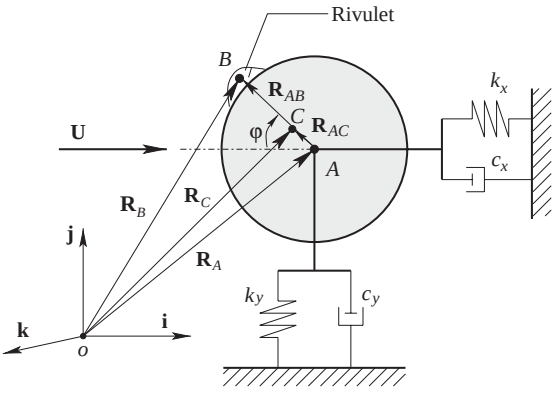

Fig. 1. Variables for Rivulet-cable model.

instantaneous rivulet section on its circumference, define position vectors:

$$\begin{aligned}\mathbf{R}_A(T) &= X(T)\mathbf{i} + Y(T)\mathbf{j},\\ \mathbf{R}_{AB}(T) &= -R\cos\varphi(T)\mathbf{i} + R\sin\varphi(T)\mathbf{j},\\ \mathbf{R}_B(T) &= \mathbf{R}_A(T) + \mathbf{R}_{AB}(T)\\ &= (X(T) - R\cos\varphi(T))\mathbf{i} + (Y(T) + R\sin\varphi(T))\mathbf{j},\end{aligned} \tag{1}$$

where T denotes time, R is constant, and φ is measured clockwise from the wind direction as shown.

The motion of the rivulet is determined by forces due to gravity, fluid–surface adhesion and friction, aerodynamic pressure and the reaction due to the motion of the cylinder to which it is attached. The latter, in turn, responds to gravity, aerodynamic pressure, mechanical forces and the contact reaction due to the rivulet. The aerodynamic torque on the rivulet section about its geometric centre is expected to be small and the torsional stiffness of the cable is sufficient to prevent significant angular motion of the disc about its centre. The equation of motion for the rivulet centre B is

$$m_r \frac{\mathrm{d}^2\mathbf{R}_B}{\mathrm{d}T^2} = \mathbf{f}_p + \mathbf{F} + \mathbf{N} + \mathbf{f}_{ad} + m_r\mathbf{g}, \tag{2}$$

where $\mathbf{f}_p$ is the total specific (i.e., per unit length) aerodynamic pressure force on the rivulet, $\mathbf{F}$ is a specific friction force tangent to the local surface of contact between rivulet and cylinder, $\mathbf{N}$ is the specific contact reaction on the rivulet directed along the outward normal to this surface and $\mathbf{f}_{ad}$ is a specific adhesion force on the rivulet directed opposite to $\mathbf{N}$. The equation for the motion of the disc centre A is

$$m \frac{\mathrm{d}^2\mathbf{R}_A}{\mathrm{d}T^2} = \mathbf{F}_p - \mathbf{F} - \mathbf{N} - \mathbf{f}_{ad} + \mathbf{K} + m\mathbf{g}, \tag{3}$$

where $\mathbf{F}_p$ is the total specific aerodynamic pressure force on the disc (excluding the rivulet) and $\mathbf{K}$ is the total specific mechanical force (including dampers) on it.

If the specific aerodynamic torque on the disc about an axis parallel to $\mathbf{k}$ through its centre is $\mathbf{M}_p$ and $\mathscr{K}$ is the specific mechanical torque on the disc about the same axis then it can execute

angular motion with angular velocity $\omega_A(T)\mathbf{k}$ determined by

$$I_A \frac{\mathrm{d}\omega_A}{\mathrm{d}T}\mathbf{k} = \mathbf{M}_p + \mathscr{K} + \mathbf{R}_{AB} \times \mathbf{F} \tag{4}$$

in terms of the specific moment of inertia I_A. Assume that torsional stiffness and damping in $\mathscr{K}$ is sufficient to suppress all angular motion about A and take $\omega_A(T) = 0$.

The aerodynamic vectors $\mathbf{F}_p(T), \mathbf{f}_p(T), \mathbf{M}_p(T)$ in (2), (3) and (4) arise from the fluid dynamics of air in the presence of moving boundaries. First model these in terms of specific forces $\mathbf{F}^{Tot}$ and torques $\mathbf{M}^{Tot}$ that may be related to wind tunnel measured data for fixed cylinders with fixed (artificial) rivulets. The relation of the orientation of such configurations (with fixed points A and B) to instantaneous configurations given by $\mathbf{R}_A(T)$ and $\mathbf{R}_B(T)$ will be discussed below. Clearly this procedure is only justified if the aerodynamic flow field around fixed configurations does not depart too much from that around moving configurations with mobile rivulets.

Under these conditions assume

$$\mathbf{F}^{Tot} \approx \mathbf{F}_p + \mathbf{f}_p, \qquad \mathbf{M}^{Tot} \approx \mathbf{M}_p + \mathbf{m}_p \tag{5}$$

where the total aerodynamic force and torque about A, acting on the disc *and* rivulet are decomposed into components acting on the disc section and rivulet, respectively. If the pressure field around the rivulet does not vary much further assume that

$$\mathbf{m}_p \approx \mathbf{R}_{AB} \times \mathbf{f}_p, \tag{6}$$

where $\mathbf{f}_p$ acts on the transverse centroid of the rivulet. Since the pressure force at any point on the disc section boundary is directed toward A then $\mathbf{M}_p = 0$ and so

$$\mathbf{M}^{Tot} \approx \mathbf{m}_p \approx \mathbf{R}_{AB} \times \mathbf{f}_p. \tag{7}$$

With these approximations one may relate components of the vectors $\mathbf{F}_p$ and $\mathbf{f}_p$ to the vectors $\mathbf{F}^{Tot}$ and $\mathbf{M}^{Tot}$. Thus if $\mathbf{n}$ denotes the unit vector in the direction of $\mathbf{N}$ and $\boldsymbol{\tau}$ is a unit vector tangential to the surface of the disc such that $\mathbf{n} \times \boldsymbol{\tau} = \mathbf{k}$, with $\mathbf{R}_{AB} = R\mathbf{n}$ and $\mathbf{f}_p = f_p^{(n)}\mathbf{n} + f_p^{(\tau)}\boldsymbol{\tau}$, it follows that

$$\begin{aligned} \mathbf{F}_p &= \mathbf{F}^{Tot} - f_p^{(n)}\mathbf{n} - \frac{M^{Tot}}{R}\boldsymbol{\tau}, \\ \mathbf{f}_p &= f_p^{(n)}\mathbf{n} + \frac{M^{Tot}}{R}\boldsymbol{\tau}, \end{aligned} \tag{8}$$

where M^{Tot} is the modulus of the torque $\mathbf{M}^{Tot}$. Inserting these into (2) and (3) gives

$$\begin{aligned} m\frac{\mathrm{d}^2\mathbf{R}_A}{\mathrm{d}T^2} &= \mathbf{F}^{Tot} - \mathscr{F} + \mathbf{K} - \mathscr{N} + m\mathbf{g}, \\ m_r\frac{\mathrm{d}^2\mathbf{R}_B}{\mathrm{d}T^2} &= \mathscr{F} + \mathscr{N} + m_r\mathbf{g}, \end{aligned} \tag{9}$$

where the tangential force $\mathscr{F}$ and the normal force $\mathscr{N}$ are

$$\begin{aligned} \mathscr{F} &= \left(F + \frac{M^{Tot}}{R}\right)\boldsymbol{\tau} \\ \mathscr{N} &= \left(N + f_{ad} + f_p^{(n)}\right)\mathbf{n} \end{aligned} \tag{10}$$

with $\mathbf{F} = F\boldsymbol{\tau}$, $\mathbf{N} = N\mathbf{n}$ and $\mathbf{f}_{ad} = f_{ad}\mathbf{n}$. Once a friction law for $\mathbf{F}$ is specified Eq. (9) can be solved for $\mathbf{R}_A(T)$, $\mathbf{R}_B(T)$ and $\mathcal{N}(T)$ in terms of data determining $\mathbf{F}^{Tot}$ and $\mathbf{M}^{Tot}$.

The force $\mathbf{K}$ includes the cable restoring force and damping. Assume that the original position of the point A (where the effective springs are un-deformed) is expressed as

$$\hat{\mathbf{R}}_A = \hat{X}\mathbf{i} + \hat{Y}\mathbf{j} \tag{11}$$

for constants $\hat{X}$ and $\hat{Y}$. Then

$$\mathbf{K} = -\left(k_x(X - \hat{X}) + c_x\frac{\mathrm{d}X}{\mathrm{d}T}\right)\mathbf{i} - \left(k_y(Y - \hat{Y}) + c_x\frac{\mathrm{d}X}{\mathrm{d}T}\right)\mathbf{j}, \tag{12}$$

where k_x and k_y denote constant horizontal and vertical stiffness parameters per unit length, and c_x and c_y denote constant structural damping parameters.

To proceed one must determine the vectors $\mathbf{F}^{Tot}$ and $\mathbf{M}^{Tot}$ as functions of the dynamic configuration of the disc and rivulet. Without fluid dynamic modelling recourse must be made to measured data. Unfortunately wind tunnel data often appears to be time averaged and restricted to cylinders where the relative motion of disc and rivulet is zero. This poses a severe limitation for the subsequent analysis of this dynamic model. Nevertheless since the initial concern is with the linearization of the equations of motion for $X(T)$, $Y(T)$ and $\varphi(T)$ about an equilibrium configuration in light wind conditions, it will be supposed that such a limitation need not inhibit further linear analysis. The strategy will be to define, for each T, a transformation to a wind tunnel frame of reference in which the flow field around a model with a fixed cylinder and fixed rivulet resembles as closely as possible an *instantaneous* flow field around the moving disc with a mobile rivulet. Clearly, away from equilibrium, there is no Galilean transformation on the dynamic disc-rivulet configuration that can identify a frame in which the velocity of the point A relative to B remains zero. In general one can apply such a transformation to a wind tunnel frame in which some preferred point C in the section model has zero velocity. The choice of C must be based on expediency. Reasons will be given below for the preferred choice $C \simeq A$.

In the following *all* quantities measured in a wind tunnel will be denoted with a ^ symbol. Thus the sum of the specific lift and drag on a fixed cylinder with centre $\hat{A}$ with a fixed rivulet with transverse centroid $\hat{B}$ is denoted $\hat{\mathbf{F}}^{Tot}$. Similarly the specific torque on it is denoted $\hat{\mathbf{M}}^{Tot}$. Let C be located at $\mathbf{R}_C$ in the inertial frame $\{\mathbf{i}, \mathbf{j}, \mathbf{k}\}$ somewhere between A and B. Then in a frame moving with velocity $\mathrm{d}\mathbf{R}_C(T)/\mathrm{d}T$ relative to this inertial frame the point C will be instantaneously at rest. In such a frame the wind will have velocity $\mathbf{U}_r = \mathbf{U} - \mathrm{d}\mathbf{R}_C/\mathrm{d}T$. To proceed assume that, for a choice of C:

$$\mathbf{F}^{Tot} \simeq \hat{\mathbf{F}}^{Tot}, \quad \mathbf{M}^{Tot} \simeq \hat{\mathbf{M}}^{Tot}. \tag{13}$$

Suppose $\hat{\alpha}$ denotes the angle (in the aerodynamic sense) between the wind tunnel inflow vector $\hat{\mathbf{U}} = \mathbf{U}_r$ and the direction $\hat{A}\hat{B}$ locating the fixed artificial rivulet and the $C_l(\hat{\alpha})$, $C_d(\hat{\alpha})$, $C_m(\hat{\alpha})$ denote the lift, drag and moment coefficients defined in the conventional manner:

$$\hat{\mathbf{F}}^{Tot} = \hat{\mathbf{f}}_d^{Tot} + \hat{\mathbf{f}}_l^{Tot} = \hat{f}_d^{Tot}\boldsymbol{\eta} + \hat{f}_l^{Tot}\boldsymbol{\zeta}, \tag{14}$$

where $\boldsymbol{\eta}$ denotes the unit vector in the direction of $\hat{\mathbf{U}}$ and $\boldsymbol{\zeta}$ is a unit vector orthogonal to $\boldsymbol{\eta}$ such that $\boldsymbol{\eta} \times \boldsymbol{\zeta} = \mathbf{k}$. Thus the modulus $\hat{f}_d^{Tot}, \hat{f}_l^{Tot}$ and $\hat{M}^{Tot}$ of vectors $\hat{\mathbf{f}}_d^{Tot}, \hat{\mathbf{f}}_l^{Tot}$ and $\hat{\mathbf{M}}^{Tot}$ are

$$\hat{f}_d^{Tot} = \tfrac{1}{2}\rho_a D\hat{U}^2 C_d(\hat{\alpha}), \quad \hat{f}_l^{Tot} = \tfrac{1}{2}\rho_a D\hat{U}^2 C_l(\hat{\alpha}), \quad \hat{M}^{Tot} = \tfrac{1}{2}\rho_a D^2\hat{U}^2 C_m(\hat{\alpha}), \tag{15}$$

where $\hat{U}$ is the modulus of the vector $\hat{\mathbf{U}}$ and $D = 2R$.

In terms of the characteristic radius $R_c = |\mathbf{R}_{AC}(T)| = AC$

$$\begin{aligned}\mathbf{R}_{AC}(T) &= -R_c\cos\varphi(T)\mathbf{i} + R_c\sin\varphi(T)\mathbf{j},\\ \mathbf{R}_C(T) &= \mathbf{R}_A(T) + \mathbf{R}_{AC}(T)\\ &= (X(T) - R_c\cos\varphi(T))\mathbf{i} + (Y(T) + R_c\sin\varphi(T)\mathbf{j}.\end{aligned} \tag{16}$$

The characteristic relative velocity $\mathbf{U}_r$ is given in terms of the inflow velocity of the wind $\mathbf{U}$ and the velocity of the characteristic point C in the original inertial frame:

$$\mathbf{U} = \mathbf{U}_r(T) + \frac{\mathrm{d}\mathbf{R}_c(T)}{\mathrm{d}T} = U\mathbf{i}. \tag{17}$$

The modulus U_r of $\mathbf{U}_r$ and the angle β as shown in Fig. 2 follow as

$$\begin{aligned}U_r^2 &= \left(U - \frac{\mathrm{d}X}{\mathrm{d}T} - R_c\frac{\mathrm{d}\varphi}{\mathrm{d}T}\sin\varphi\right)^2 + \left(\frac{\mathrm{d}Y}{\mathrm{d}T} + R_c\frac{\mathrm{d}\varphi}{\mathrm{d}T}\cos\varphi\right)^2,\\ \tan\beta &= \frac{\frac{\mathrm{d}Y}{\mathrm{d}T} + R_c\frac{\mathrm{d}\varphi}{\mathrm{d}T}\cos\varphi}{U - \frac{\mathrm{d}X}{\mathrm{d}T} - R_c\frac{\mathrm{d}\varphi}{\mathrm{d}T}\sin\varphi}.\end{aligned} \tag{18}$$

The angle of attack $\hat{\alpha}$ in the wind tunnel is simply related to the angle β between $\mathbf{U}$ and $\mathbf{U}_r$ (see Fig. 2(b)):

$$\hat{\alpha} = \varphi - \beta. \tag{19}$$

Thus one has $\mathbf{U}_r$ and β as functions of $\varphi, \mathrm{d}\varphi/\mathrm{d}T, \mathrm{d}X/\mathrm{d}T, \mathrm{d}Y/\mathrm{d}T, U, R_c$ and similarly for $|\hat{\mathbf{U}}|$ and $\hat{\alpha}$ that connect the data in the aerodynamic coefficients C_l, C_d, C_m to the dynamical variables for given U and R_c.

Taking notice of

$$\begin{aligned}\mathbf{n} &= -\cos\varphi\mathbf{i} + \sin\varphi\mathbf{j}, \quad \boldsymbol{\eta} = \cos\beta\mathbf{i} - \sin\beta\mathbf{j},\\ \boldsymbol{\tau} &= -\sin\varphi\mathbf{i} - \cos\varphi\mathbf{j}, \quad \boldsymbol{\zeta} = \sin\beta\,\mathbf{i} + \cos\beta\,\mathbf{j}\end{aligned} \tag{20}$$

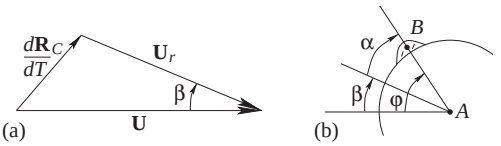

Fig. 2. Characteristic relative velocity and the angle of attack.

and substituting (1), (10), (12), (13) and (14) into the equations of motion (9) yields:

$$
\begin{aligned}
&m\frac{\mathrm{d}^2X}{\mathrm{d}T^2}+c_x\frac{\mathrm{d}X}{\mathrm{d}T}+k_x(X-\hat{X})\\
&\quad=\hat{f}_d^{Tot}\cos\beta+\hat{f}_l^{Tot}\sin\beta+\left(F+\frac{M^{Tot}}{R}\right)\sin\varphi+(N+f_{ad}+f_p^{(n)})\cos\varphi,\\
&m\frac{\mathrm{d}^2Y}{\mathrm{d}T^2}+c_y\frac{\mathrm{d}Y}{\mathrm{d}T}+k_y(Y-\hat{Y})\\
&\quad=-\hat{f}_d^{Tot}\sin\beta+\hat{f}_l^{Tot}\cos\beta+\left(F+\frac{M^{Tot}}{R}\right)\cos\varphi-(N+f_{ad}+f_p^{(n)})\sin\varphi-mg,\\
&m_r\frac{\mathrm{d}^2X}{\mathrm{d}T^2}+m_rR\frac{\mathrm{d}^2\varphi}{\mathrm{d}T^2}\sin\varphi+m_rR\left(\frac{\mathrm{d}\varphi}{\mathrm{d}T}\right)^2\cos\varphi\\
&\quad=-(N+f_{ad}+f_p^{(n)})\cos\varphi-\left(F+\frac{M^{Tot}}{R}\right)\sin\varphi,\\
&m_r\frac{\mathrm{d}^2Y}{\mathrm{d}T^2}+m_rR\frac{\mathrm{d}^2\varphi}{\mathrm{d}T^2}\cos\varphi-m_rR\left(\frac{\mathrm{d}\varphi}{\mathrm{d}T}\right)^2\sin\varphi\\
&\quad=(N+f_{ad}+f_p^{(n)})\sin\varphi-\left(F+\frac{M^{Tot}}{R}\right)\cos\varphi-m_rg.
\end{aligned}
\tag{21}
$$

From the last two equations of (21), the normal force follows as

$$
\begin{aligned}
\mathcal{N}&=(N+f_{ad}+f_p^{(n)})\mathbf{n}\\
&=\left(m_r\left(g+\frac{\mathrm{d}^2Y}{\mathrm{d}T^2}\right)\sin\varphi-m_r\frac{\mathrm{d}^2X}{\mathrm{d}T^2}\cos\varphi-m_rR\left(\frac{\mathrm{d}\varphi}{\mathrm{d}T}\right)^2\right)\mathbf{n}.
\end{aligned}
\tag{22}
$$

Substituting (22) into (21) then gives

$$
\begin{aligned}
&(m+m_r)\frac{\mathrm{d}^2X}{\mathrm{d}T^2}+m_rR\frac{\mathrm{d}^2\varphi}{\mathrm{d}T^2}\sin\varphi+m_rR\left(\frac{\mathrm{d}\varphi}{\mathrm{d}T}\right)^2\cos\varphi+c_x\frac{\mathrm{d}X}{\mathrm{d}T}+k_x(X-\hat{X})\\
&\quad=\hat{f}_d^{Tot}\cos\beta+\hat{f}_l^{Tot}\sin\beta,\\
&(m+m_r)\frac{\mathrm{d}^2Y}{\mathrm{d}T^2}+m_rR\frac{\mathrm{d}^2\varphi}{\mathrm{d}T^2}\cos\varphi-m_rR\left(\frac{\mathrm{d}\varphi}{\mathrm{d}T}\right)^2\sin\varphi+c_y\frac{\mathrm{d}Y}{\mathrm{d}T}+k_y(Y-\hat{Y})\\
&\quad=-\hat{f}_d^{Tot}\sin\beta+\hat{f}_l^{Tot}\cos\beta-(m+m_r)g,\\
&m_r\frac{\mathrm{d}^2X}{\mathrm{d}T^2}\sin\varphi+m_r\frac{\mathrm{d}^2Y}{\mathrm{d}T^2}\cos\varphi+m_rR\frac{\mathrm{d}^2\varphi}{\mathrm{d}T^2}=-F-\frac{M^{Tot}}{R}-m_rg\cos\varphi.
\end{aligned}
\tag{23}
$$

With $\omega=\sqrt{k_x/(m+m_r)}$, introduce the following non-dimensional quantities:

$$
\gamma=\sqrt{\frac{k_y}{k_x}},\quad t=\omega T,\quad \mu_1=\frac{m_r}{2(m+m_r)},
$$

$$\xi_x = \frac{c_x}{2(m+m_r)\omega}, \quad \xi_y = \frac{c_y}{2(m+m_r)\gamma\omega},$$
$$x = \frac{X}{D}, \quad y = \frac{Y}{D}, \quad \hat{x} = \frac{\hat{X}}{D}, \quad \hat{y} = \frac{\hat{Y}}{D}. \tag{24}$$

Then (23) can be written as the system:

$$\begin{aligned}
&\ddot{x} + \mu_1\ddot{\varphi}\sin\varphi + \mu_1\dot{\varphi}^2\cos\varphi + 2\xi_x\dot{x} + x \\
&\quad = \hat{x} + \frac{\hat{f}_d^{Tot}\cos\beta + \hat{f}_l^{Tot}\sin\beta}{(m+m_r)D\omega^2}, \\
&\ddot{y} + \mu_1\ddot{\varphi}\cos\varphi - \mu_1\dot{\varphi}^2\sin\varphi + 2\xi_y\gamma\dot{y} + \gamma^2 y \\
&\quad = \gamma^2\hat{y} + \frac{\hat{f}_l^{Tot}\cos\beta - \hat{f}_d^{Tot}\sin\beta}{(m+m_r)D\omega^2} - \frac{g}{D\omega^2}, \\
&\ddot{\varphi} + 2\ddot{x}\sin\varphi + 2\ddot{y}\cos\varphi = -\frac{RF + \hat{M}^{Tot}}{m_r R^2\omega^2} - \frac{2g}{D\omega^2}\cos\varphi,
\end{aligned} \tag{25}$$

where $(\dot{})$ denotes differentiation with respect to the dimensionless time parameter t.

Let $\phi(t) = \varphi(t) - \varphi_0$, where $\phi(t)$ defines the fluctuation angle of an oscillating rivulet around an equilibrium location angle φ_0 on the cable perimeter. Assume that the friction force F can be written

$$F = F_0 + c_\phi\frac{\mathrm{d}\phi}{\mathrm{d}T} = F_0 + c_\phi\omega\dot{\phi}, \tag{26}$$

where the constant

$$F_0 = -m_r g\cos\varphi_0 - \rho_a D U^2 C_m(\varphi_0) \tag{27}$$

ensures that $\varphi = \varphi_0$ is an equilibrium position. The constant c_ϕ is related to the thickness of the rivulet, the density of the liquid, the surface roughness and the surface material of the cable.

For convenience introduce f_x and f_y as

$$\begin{aligned}
f_x &= \hat{f}_l^{Tot}\sin\beta + \hat{f}_d^{Tot}\cos\beta = \tfrac{1}{2}\rho_a D U_r^2(C_l(\hat{\alpha})\sin\beta + C_d(\hat{\alpha})\cos\beta), \\
f_y &= \hat{f}_l^{Tot}\cos\beta - \hat{f}_d^{Tot}\sin\beta = \tfrac{1}{2}\rho_a D U_r^2(C_l(\hat{\alpha})\cos\beta - C_d(\hat{\alpha})\sin\beta),
\end{aligned} \tag{28}$$

where the angle of attack $\hat{\alpha}(\varphi,\beta) = \varphi - \beta$, and where the dynamic relative wind angle β is a function of $\varphi, \dot{x}, \dot{y}$ and $\dot{\varphi}$. Substituting (18) into (28) and expanding the dynamic forces $f_x(\phi,\dot{x},\dot{y},\dot{\phi})$, $f_y(\phi,\dot{x},\dot{y},\dot{\phi})$ and $\hat{M}^{Tot}(\phi,\dot{x},\dot{y},\dot{\phi})$ as a Taylor expansion with respect to the variables $(\phi,\dot{x},\dot{y},\dot{\phi})$ about the equilibrium $(0,0,0,0)$ (i.e., $\hat{\alpha} = \varphi_0$), yields:

$$\begin{aligned}
f_x(\phi,\dot{x},\dot{y},\dot{\phi}) = &\tfrac{1}{2}\rho_a D U^2[C_d(\varphi_0) + C_d'(\varphi_0)\phi] \\
&+ \tfrac{1}{2}\rho_a\omega D R_c U[(C_l(\varphi_0) - C_d'(\varphi_0))\cos\varphi_0 - 2C_d(\varphi_0)\sin\varphi_0]\dot{\phi} \\
&- \tfrac{1}{2}\rho_a\omega D^2 U[2C_d(\varphi_0)\dot{x} - (C_l(\varphi_0) - C_d'(\varphi_0))\dot{y}] + h_x(\phi,\dot{x},\dot{y},\dot{\phi}),
\end{aligned} \tag{29}$$

$$
\begin{aligned}
f_y(\phi,\dot{x},\dot{y},\dot{\phi}) = & \tfrac{1}{2}\rho_a D U^2[C_l(\varphi_0) + C_l'(\varphi_0)\phi] \\
& - \tfrac{1}{2}\rho_a \omega D R_c U[(C_d(\varphi_0) + C_l'(\varphi_0))\cos\varphi_0 + 2C_l(\varphi_0)\sin\varphi_0]\dot{\phi} \\
& - \tfrac{1}{2}\rho_a \omega D^2 U[2C_l(\varphi_0)\dot{x} + (C_d(\varphi_0) + C_l'(\varphi_0))\dot{y}] + h_y(\phi,\dot{x},\dot{y},\dot{\phi}),
\end{aligned} \tag{30}
$$

$$
\begin{aligned}
\hat{M}^{Tot}(\phi,\dot{x},\dot{y},\dot{\phi}) = & -\tfrac{1}{2}\rho_a D^2 U^2[C_m(\varphi_0) + C_m'(\varphi_0)\phi] \\
& + \tfrac{1}{2}\rho_a \omega D^2 R_c U[C_m'(\varphi_0)\cos\varphi_0 + 2C_m(\varphi_0)\sin\varphi_0]\dot{\phi} \\
& + \tfrac{1}{2}\rho_a \omega D^3 U[2C_m(\varphi_0)\dot{x} + C_m'(\varphi_0)\dot{y}] + h_m(\phi,\dot{x},\dot{y},\dot{\phi}),
\end{aligned} \tag{31}
$$

where $(')$ denotes differentiation with respect to the angle $\hat{\alpha}$. The terms $h_x(\phi,\dot{x},\dot{y},\dot{\phi})$, $h_y(\phi,\dot{x},\dot{y},\dot{\phi})$ and $h_m(\phi,\dot{x},\dot{y},\dot{\phi})$ contain non-linear functions of $\phi,\dot{x},\dot{y},\dot{\phi}$.

Let $\mathbf{z} = [x,\ y,\ \phi]^{\mathrm{T}}$ and

$$
\begin{aligned}
&\mu_2 = \frac{g}{R\omega^2}, \quad \xi_\phi = \frac{c_\phi}{2m_r R\omega}, \quad \mu_3 = \frac{\rho_a D U}{2(m+m_r)\omega}, \\
&\mu_4 = \frac{2\rho_a D U}{m_r \omega}, \quad \mu_5 = \frac{R_c}{D} \quad \mu_6 = \frac{U}{\omega D},
\end{aligned} \tag{32}
$$

so that (25) can be written as

$$
\mathbf{G}_m\ddot{\mathbf{z}}(t) + \mathbf{G}_d\dot{\mathbf{z}}(t) + \mathbf{G}_k\mathbf{z}(t) = \mathbf{b} + \mathbf{h}(\mathbf{z},\dot{\mathbf{z}}), \tag{33}
$$

where $\mathbf{h}(\mathbf{z},\dot{\mathbf{z}})$ is a non-linear vector function representing second and higher order terms in $\phi,\dot{x},\dot{y}$ and $\dot{\phi}$,

$$
\begin{aligned}
\mathbf{G}_m &= \begin{bmatrix} 1 & 0 & \mu_1\sin\varphi_0 \\ 0 & 1 & \mu_1\cos\varphi_0 \\ 2\sin\varphi_0 & 2\cos\varphi_0 & 1 \end{bmatrix}, \\
\mathbf{G}_k &= \begin{bmatrix} 1 & 0 & -\mu_3\mu_6 C_d'(\varphi_0) \\ 0 & \gamma^2 & -\mu_3\mu_6 C_l'(\varphi_0) \\ 0 & 0 & \mu_4\mu_6 C_m'(\varphi_0) - \mu_2\sin\varphi_0 \end{bmatrix}, \\
\mathbf{b} &= \begin{bmatrix} \hat{x} + \mu_3\mu_6 C_d(\varphi_0) \\ \gamma^2\hat{y} + \mu_3\mu_6 C_l(\varphi_0) - \tfrac{1}{2}\mu_2 \\ 0 \end{bmatrix},
\end{aligned} \tag{34}
$$

and

$$
\begin{aligned}
\mathbf{G}_d = \begin{bmatrix} 2\xi_x + 2\mu_3 C_d(\varphi_0) & \mu_3(C_d'(\varphi_0) - C_l(\varphi_0)) \\ 2\mu_3 C_l(\varphi_0) & 2\xi_y\gamma + \mu_3(C_d(\varphi_0) + C_l'(\varphi_0)) \\ -2\mu_4 C_m(\varphi_0) & -\mu_4 C_m'(\varphi_0) \end{bmatrix} \\
\begin{matrix} \mu_3\mu_5[2C_d(\varphi_0)\sin\varphi_0 + (C_d'(\varphi_0) - C_l(\varphi_0))\cos\varphi_0] \\ \mu_3\mu_5[2C_l(\varphi_0)\sin\varphi_0 + (C_d(\varphi_0) + C_l'(\varphi_0))\cos\varphi_0] \\ 2\xi_\phi - \mu_4\mu_5[2C_m(\varphi_0)\sin\varphi_0 + C_m'(\varphi_0)\cos\varphi_0] \end{matrix}
\end{aligned} \tag{35}
$$

The equilibrium state in terms of $\mathbf{z}(t)$ and $\dot{\mathbf{z}}(t)$ is

$$\mathbf{z}(t) = \mathbf{z}_0 = \mathbf{G}_k^{-1}\mathbf{b} = \begin{bmatrix} \hat{x} + \mu_3\mu_6 C_d(\varphi_0) \\ \hat{y} + \dfrac{2\mu_3\mu_6 C_l(\varphi_0) - \mu_2}{2\gamma^2} \\ 0 \end{bmatrix} = \begin{bmatrix} x_0 \\ y_0 \\ 0 \end{bmatrix}, \quad \dot{\mathbf{z}}(t) = 0. \tag{36}$$

Linearized stability follows by writing

$$\mathbf{z}(t) = \mathbf{z}_0 + \tilde{\mathbf{z}}(t). \tag{37}$$

So

$$\dot{\mathbf{w}}(t) = \mathbf{G}\mathbf{w}(t), \tag{38}$$

where

$$\mathbf{w} = \begin{bmatrix} \tilde{\mathbf{z}} \\ \dot{\tilde{\mathbf{z}}} \end{bmatrix}, \quad \mathbf{G} = \begin{bmatrix} \mathbf{0} & \mathbf{I} \\ -\mathbf{G}_m^{-1}\mathbf{G}_k & -\mathbf{G}_m^{-1}\mathbf{G}_d \end{bmatrix}, \tag{39}$$

and $\mathbf{I}$ is the 3×3 identity matrix.

Solutions to the system (38) govern the small amplitude wind-rain induced vibrations in the deterministic model. By adding linear stochastic terms a stochastic model arises along the lines discussed in Ref. [11].

The circumferential oscillations of the rivulet and the transverse oscillations of the cable are completely coupled due to the coupled mass, damping and stiffness matrices. The onset of unstable, aerodynamically induced vibration is determined by the eigenvalues of the system matrix $\mathbf{G}$. The equilibrium state is stable at the linearized level if and only if all eigenvalues of $\mathbf{G}$ have negative real parts, i.e., $\mathbf{G}$ is a Hurwitz matrix. The equilibrium state is unstable if at least one of the eigenvalues of $\mathbf{G}$ has a positive real part. The equilibrium state is critical if all eigenvalues of $\mathbf{G}$ have non-positive real parts and there exists at least one critical eigenvalue (having zero real part).

Linearized stability conditions can be determined by the Hurwitz criterion [24] without actually solving the full eigenvalue problem. However, the determination of the eigenvalues and the corresponding eigenvectors of the system matrix $\mathbf{G}$ provides valuable insights into the behaviour of the wind-rain induced vibrations under discussion. It is convenient to introduce a measure that indicates the nature of the normal mode associated with any particular eigenvector ψ_j with components ψ_{jk} and complex conjugate transpose $\psi_j^\dagger$. In particular, for $j = 1, 2, \ldots, 6$ let

$$\delta_j = \frac{|\psi_{j3}|^2 + |\psi_{j6}|^2}{\psi_j^\dagger \psi_j}$$

be a measure of the torsional content associated with the eigenvector ψ_j.

If $\delta_j \simeq 1$, the corresponding jth eigenmode is dominated by the circumferential motion of the rivulet. If $\delta_j \simeq 0$, the corresponding eigenmode is dominated by the translational motion of the cable. Depending on initial conditions of course, a general motion will be a superposition of such eigenmodes.

The details of this model include a choice for the parameter R_c. Yamaguchi [5] asserted that the relative velocity $\mathbf{U}_r$ is characterized only by the speed of the rivulet and he took $R_c = R$, the radius of the cross-section of the cable. In the model here the appropriate choice is dependent on the damping parameters and the nature of the rivulet. Based on an analysis of this linearized system for a range of such parameters and the observed data for the onset of wind-rain induced vibrations, it is evident that R_c should be small compared to the cable radius and related to the thickness of the rivulet. The effects of R_c on the behaviour of the system are discussed in the following and it is concluded that $R_c \simeq 0$ is a better choice under realistic light wind conditions for both mechanically light and heavily damped cables.

3. Numerical results and discussion

Analyzing the dynamic behaviour of the system from the linearized perspective requires the determination of the eigenvalues and eigenvectors of the system matrix. In this section, numerical calculations based on (38) are carried out using the following parameters. The diameter D and the mass m per unit length of the stay cable are chosen as 180 mm and 68 kg/m, respectively. The air density is taken as 1.293 kg/m^3. The cable is assumed to be at the first "cross-over" point [25], so that the frequency ratio of the first in-plane mode to the first out-of-plane mode is almost 2.0. The lateral stiffness of the cable per unit length, k_x, is assumed to be 1600 N/m^2, and $\gamma = 2.2$. Thus, $\omega = \sqrt{k_x/(m + m_r)} = 4.833$ rad/s.

The appropriate (time averaged) drag, lift and moment coefficients for a cylinder with a fixed upper artificial rivulet are taken from wind tunnel tests. Experimental values of such steady wind force coefficients for an aluminium circular cylinder with a fixed artificial rivulet (a solid cylinder of diameter d with $d/D = 0.1$), were reported in [5] as shown in Fig. 3.[1] The aerodynamic coefficient curves depicted in Fig. 3 are fitted first to express the coefficients as the functions of the attack angle α and then to obtain the derivatives of different orders. The ratio, $d/D = 0.1$, was chosen in [5] for studying the effects of such an artificial rivulet on cable forces in a steady wind. Such a ratio is probably rather large in the context of a rain rivulet in a stay cable. Based on this ratio and assuming that the density of water is 1000 kg/m^3, the mass of the rivulet per unit length is calculated to be 0.254 kg/m.

According to wind tunnel tests that reproduce rain conditions [1], the static angle φ_0 of the rivulet[2] is a function of the mean wind speed U, as shown in Fig. 4.

Employing the relation between the static angle φ_0 of the rivulet and mean wind speed, the entries of the system matrix $\mathbf{G}$ are functions of mean wind speed U, damping coefficients c_x, c_y, c_ϕ and the characteristic radius R_c. Suppose, for some particular integer m, the eigenvalue λ_m has the largest real part in the spectrum and write:

$$\delta \equiv \delta_m, \quad \Lambda(U, R_c) \equiv \mathscr{R}(\lambda_m(U, R_c)). \tag{40}$$

The quantity Λ will be referred to as the stability index and δ as the eigenmode character.

[1] The reference position of the angle of attack is different from that in Ref. [5].

[2] The reference position φ_0 is different from that in Ref. [1].

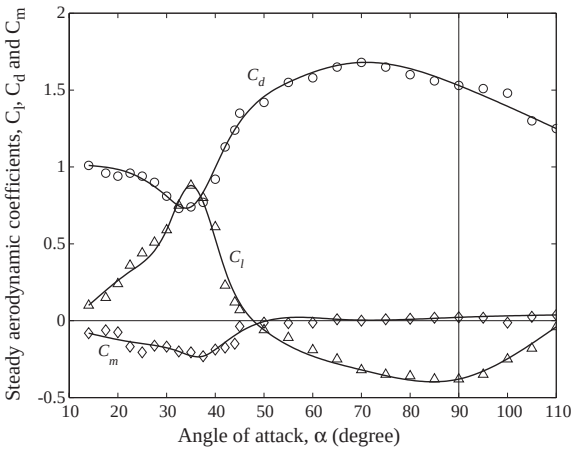

Fig. 3. Aerodynamic coefficients for a section model with an artificial rivulet.

For a lightly damped cable the structural damping coefficients are assumed to be $c_x = 0.96$ N s/m^2 and $c_y = 0.96\gamma = 2.112$ N s/m^2 corresponding to a 0.15% damping ratio. The viscous damping coefficient between the rivulet and cable surface upon which it rests, c_ϕ, is assumed to be 0.01 N s/m throughout. For such damping coefficients the stability domain $\Lambda(U, R_c) < 0$ depicted in Fig. 5 shows the effect of mean wind speed U from 9 m/s to 16 m/s and the characteristic radius $R_c \leqslant 0.012$ m on linearized stability. Thus the motion of the coupled cable-rivulet system is stable in the range of wind speed from 9.3 to 12.5 m/s for small characteristic radius R_c. The value of $\Lambda(U, R_c)$ increases as R_c increases in the stable range of wind speed. When R_c becomes large enough ($R_c > 0.012$ m $= 2R/15$) the system becomes (linearly) unstable except for a small range of wind speed around 12.5 m/s. Large amplitude wind-rain oscillations of cables with $R = 0.09$ m have been observed to develop only at certain wind tunnel speeds. These would not be predicted in the model if the characteristic radius R_c were chosen to be close to R at this damping level.

Information about the eigenvector characteristics can be inferred from the corresponding value of δ shown in Fig. 6. It can be seen from Figs. 5 and 6 that, for most points in the unstable range, δ is greater than 0.9.

It is worth noting that the eigen-behaviour is dominated by the circumferential motion of the rivulet in the unstable region except for two small ranges which are depicted in detail in Fig. 7. When the system is unstable and dominated by the circumferential motion of the rivulet, the rivulet may move to a new equilibrium state or break contact with the cable, depending on the value of normal force $\mathcal{N}$. Thus, the "unstable" regions where $\delta \simeq 1$ should not be interpreted as domains necessarily leading to large amplitude oscillations of the stay cable. On the other hand for $\delta < 0.9$ say, in such a domain, an initial displacement and/or velocity of the rivulet might cause large amplitude oscillation of the cable. According to the model this could occur with wind speeds between 9.25 and 9.26 m/s and in the interval from 12.60 to 12.64 m/s as shown in Fig. 7.

These general considerations are borne out in numerical simulations based on the linearized equation (38). In the following figures one may observe how certain initial conditions determine the onset of vibration and how such vibrations are dominated by certain eigen-modes. With

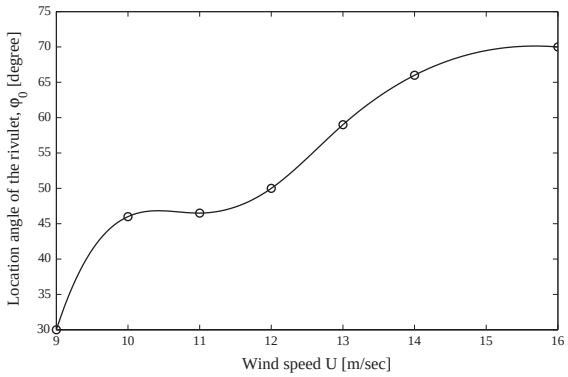

Fig. 4. Equilibrium Rivulet position versus wind speed.

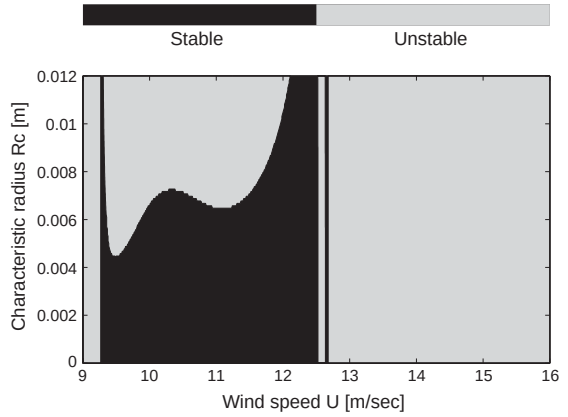

Fig. 5. Stability range ($\Lambda(U, R_c) < 0$) for coupled cable-rivulet model. $c_x = 0.96$ N s/m^2, $c_y = 0.96\gamma$ N s/m^2 and $c_\phi = 0.01$ N s/m.

$X_0 = Dx_0$ and $Y_0 = Dy_0$ where x_0 and y_0 are given by (36), displacement time histories are shown in Figs. 8 and 9 for wind speeds $U = 9.254$ and 12.605 m/s and $R_c = 0.0$, respectively. The same initial conditions $X(0) - X_0 = Y(0) - Y_0 = 0.0, \phi(0) = 0.1$ rad and $(\mathrm{d}X/\mathrm{d}T)(0) = (\mathrm{d}Y/\mathrm{d}T)(0) = (\mathrm{d}\phi/\mathrm{d}T)(0) = 0$ were assumed to illustrate the initiation of cable oscillations from an initial angular position of the rivulet. Both $U = 9.254$ m/s and $U = 12.605$ m/s with $R_c = 0.0$ are located in the unstable region with $\delta \leqslant 0.9$. From Figs. 8 and 9 it can be seen that the growing transverse oscillations of the cable are generated from an initial circumferential displacement of the rivulet.

Fig. 10 shows the displacement time histories for wind speed $U = 12.68$ m/s and characteristic radius $R_c = 0.0$ with initial conditions of $X(0) - X_0 = 0.009$ m, $Y(0) - Y_0 = 0.009$ m, $\phi(0) = 0.1$ rad and $(\mathrm{d}X/\mathrm{d}T)(0) = (\mathrm{d}Y/\mathrm{d}T)(0) = (\mathrm{d}\phi/\mathrm{d}T)(0) = 0$. In this case the circumferential motion of the rivulet is not oscillatory and the amplitude increases. In the linearized approximation such behaviour is valid as long as both $D\omega\dot{x}/U$ and $D\omega\dot{y}/U$ are small.

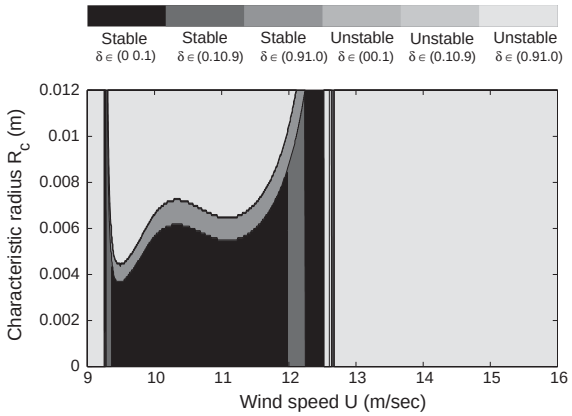

Fig. 6. Contour plane for stability index Λ and eigenmode character δ. $c_x = 0.96$ N s/m^2, $c_y = 0.96\gamma$ N s/m^2 and $c_\phi = 0.01$ N s/m.

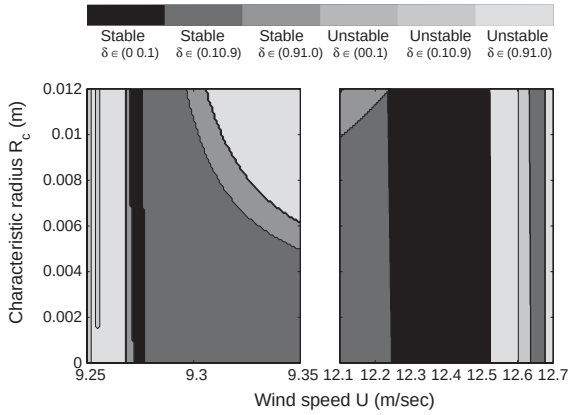

Fig. 7. Contour plane for stability index Λ and eigenmode character δ. $c_x = 0.96$ N s/m^2, $c_y = 0.96\gamma$ N s/m^2 and $c_\phi = 0.01$ N s/m.

Displacement time histories are shown in Figs. 11–13 for wind speed $U = 10.50$ m/s with $R_c = 0.0, R_c = 0.005$ m $= 0.055R$, and $R_c = 0.01$ m $= 0.11R$, respectively. The same initial conditions $X(0) - X_0 = Y(0) - Y_0 = 0.0$, $\phi(0) = 0.1$ rad and $(\mathrm{d}X/\mathrm{d}T)(0) = (\mathrm{d}Y/\mathrm{d}T)(0) = (\mathrm{d}\phi/\mathrm{d}T)(0) = 0$ have been used in the simulations. Both cases of $R_c = 0.0$ and 0.005 are located in the stable range. From Figs. 11 and 12 it can be seen that, in this situation, the system is stable.

As the characteristic radius R_c increases for the damping considered, however, the system becomes unstable. The case of $U = 10.50$ m/s with $R_c = 0.01$ m is located in the unstable range with eigenmode character $\delta > 0.9$. In this case the amplitude of the circumferential oscillation of the rivulet increases with time, while the transverse oscillation of the cable are non-increasing in the first 50 s as shown in Fig. 13.

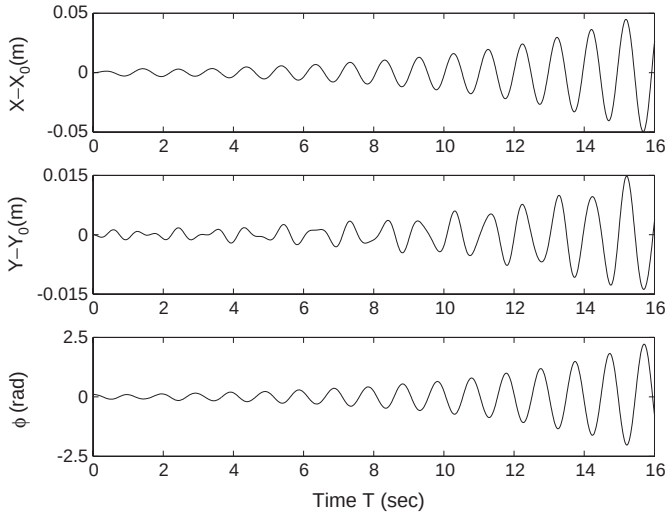

Fig. 8. Displacement time histories for wind speed $U = 9.254$ m/s and characteristic radius $R_c = 0.0$ with initial conditions of $X(0) - X_0 = 0.0$, $Y(0) - Y_0 = 0$, $\phi(0) = 0.1$ rad and $(\mathrm{d}X/\mathrm{d}T)(0) = (\mathrm{d}Y/\mathrm{d}T)(0) = (\mathrm{d}\phi/\mathrm{d}T)(0) = 0$. $c_x = 0.96$ N s/m^2, $c_y = 0.96\gamma$ N s/m^2 and $c_\phi = 0.01$ N s/m.

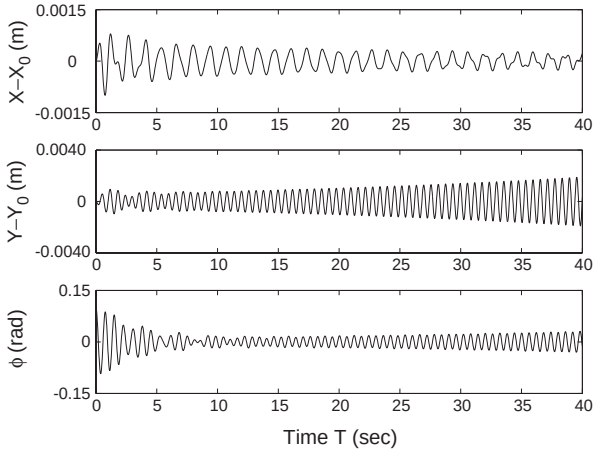

Fig. 9. Displacement time histories for wind speed $U = 12.605$ m/s and characteristic radius $R_c = 0.0$ with initial displacements of $X(0) - X_0 = 0.0$, $Y(0) - Y_0 = 0$, $\phi(0) = 0.1$ rad and $(\mathrm{d}X/\mathrm{d}T)(0) = (\mathrm{d}Y/\mathrm{d}T)(0) = (\mathrm{d}\phi/\mathrm{d}T)(0) = 0$. $c_x = 0.96$ N s/m^2, $c_y = 0.96\gamma$ N s/m^2 and $c_\phi = 0.01$ N s/m.

The effect of mechanical damping on the system is determined by the parameters c_x, c_y, and c_ϕ. The stability domains for larger values of R_c and larger damping than indicated in the corresponding Figs. 5–13 have been calculated and results displayed in Figs. 14 and 15 for comparison. It can be seen that as the characteristic radius R_c increases the more heavily damped system can still become unstable.

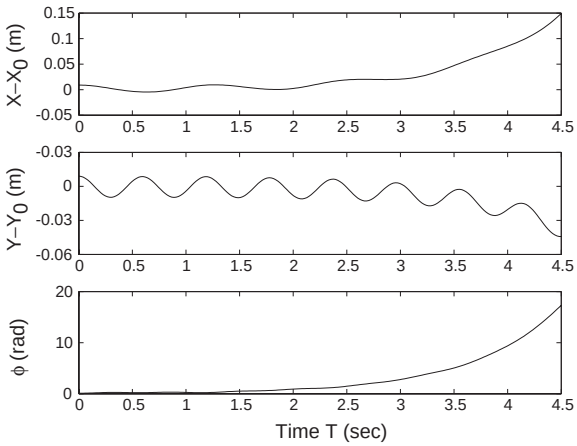

Fig. 10. Displacement time histories for wind speed $U = 12.68$ m/s and characteristic radius $R_c = 0.0$ with initial displacements of $X(0) - X_0 = 0.009$ m, $Y(0) - Y_0 = 0.009$ m, $\phi(0) = 0.1$ rad and $(\mathrm{d}X/\mathrm{d}T)(0) = (\mathrm{d}Y/\mathrm{d}T)(0) = (\mathrm{d}\phi/\mathrm{d}T)(0) = 0$. $c_x = 0.96$ N s/m^2, $c_y = 0.96\gamma$ N s/m^2 and $c_\phi = 0.01$ N s/m.

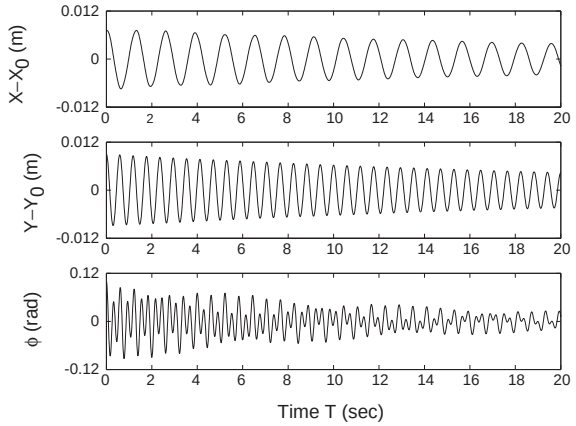

Fig. 11. Displacement time histories for wind speed $U = 10.50$ ms and characteristic radius $R_c = 0.0$ with initial displacements of $X(0) - X_0 = 0.0072$ m, $Y(0) - Y_0 = 0.009$ m, $\phi(0) = 0.1$ rad and $(\mathrm{d}X/\mathrm{d}T)(0) = (\mathrm{d}Y/\mathrm{d}T)(0) = (\mathrm{d}\phi/\mathrm{d}T)(0) = 0$. $c_x = 0.96$ N s/m^2, $c_y = 0.96\gamma$ N s/m^2 and $c_\phi = 0.01$ N s/m.

4. Estimate of aerodynamic forces and torques from vortex methods

The model constructed above relies on *time averaged* wind-tunnel data for the aerodynamic forces $\mathbf{F}_p, \mathbf{f}_p$ and torque $\mathbf{M}_p$. This data has been extracted from a series of specific forces $\mathbf{F}^{Tot}$ and torques $\mathbf{M}^{Tot}$ derived from measurements on *fixed* cylinders with *fixed* (artificial) rivulets. In order to effect this extraction one assumes that the aerodynamic flow around such fixed configurations does not depart too much from that around moving configurations with attached mobile rivulets. One way to test this hypothesis would be to employ computational fluid dynamics in conjunction with the equations of motion derived in Section 2 to calculate $\mathbf{F}_p, \mathbf{f}_p, \mathbf{M}_p$ in the presence of moving

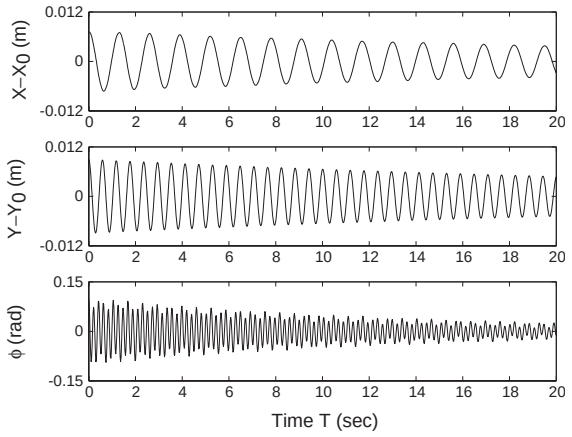

Fig. 12. Displacement time histories for wind speed $U = 10.50$ m/s and characteristic radius $R_c = 0.005$ m with initial displacements of $X(0) - X_0 = 0.0072$ m, $Y(0) - Y_0 = 0.009$ m, $\phi(0) = 0.1$ rad and $(\mathrm{d}X/\mathrm{d}T)(0) = (\mathrm{d}Y/\mathrm{d}T)(0) = (\mathrm{d}\phi/\mathrm{d}T)(0) = 0$. $c_x = 0.96$ N s/m^2, $c_y = 0.96\gamma$ N s/m^2 and $c_\phi = 0.01$ N s/m.

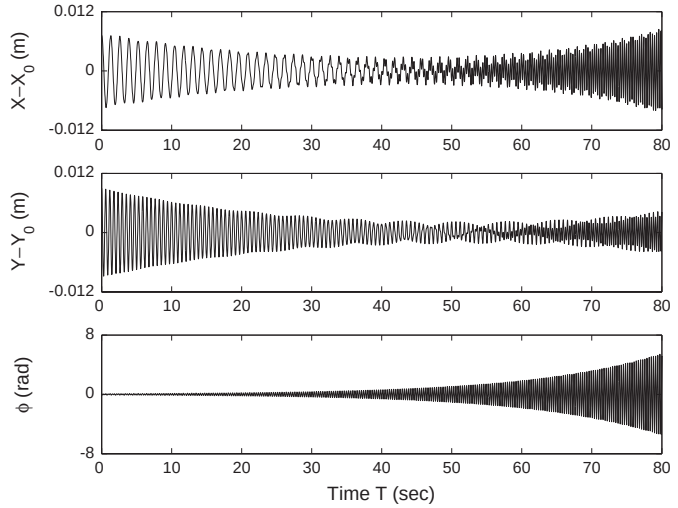

Fig. 13. Displacement time histories for wind speed $U = 10.50$ m/s and characteristic radius $R_c = 0.01$ m with initial displacements of $X(0) - X_0 = 0.0072$ m, $Y(0) - Y_0 = 0.009$ m, $\phi(0) = 0.1$ rad and $(\mathrm{d}X/\mathrm{d}T)(0) = (\mathrm{d}Y/\mathrm{d}T)(0) = (\mathrm{d}\phi/\mathrm{d}T)(0) = 0$. $c_x = 0.96$ N s/m^2, $c_y = 0.96\gamma$ N s/m^2 and $c_\phi = 0.01$ N s/m.

boundaries. Such a calculation would be computationally intensive and time consuming. However, for the light winds under consideration the Reynolds number of relevance to this problem is expected to be sub-critical and "discrete vortex" methods (see Ref. [26] for a review) in an inviscid incompressible fluid offer a viable alternative. In such an approach a simple two-dimensional boundary layer model can be used to estimate the dynamical position of points on the disc perimeter where boundary layer separation occurs. Such points can be used to locate the

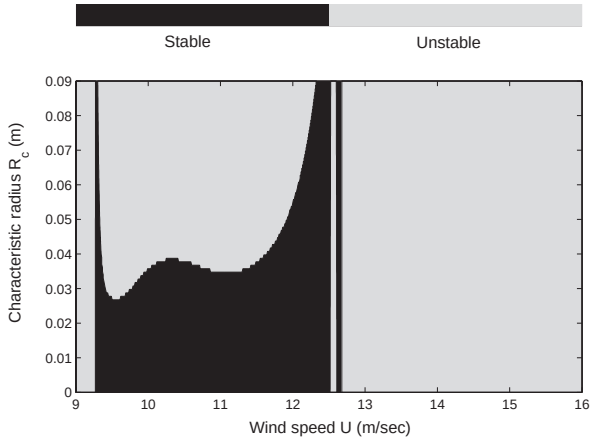

Fig. 14. Stability range ($\Lambda(U, R_c)<0$) for coupled cable-rivulet model. $c_x = 4.80$ N s/m^2, $c_y = 4.80\gamma$ N s/m^2, $c_\phi = 0.05$ N s/m.

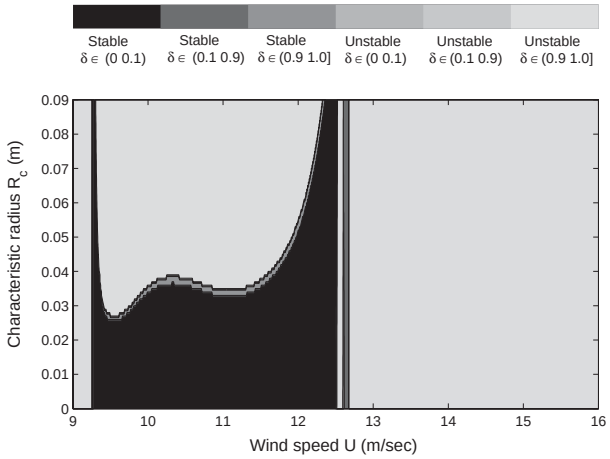

Fig. 15. Contour plane for stability index Λ and eigenmode character δ. $c_x = 4.80$ N s/m^2, $c_y = 4.80\gamma$ N s/m^2, $c_\phi = 0.05$ N s/m.

emission of vorticity (using the ''no-slip'' boundary conditions at the moving boundary [27]) in the form of point vortices (see Fig. 16).

By superposing a series of such fluid configurations on the incident wind flow one may construct a dynamic model of the flow around a moving disc with a (small) mobile rivulet. The corresponding pressure field may be used at each instant to calculate the aerodynamic forces and torques on the cylinder-rivulet system which then responds dynamically according to the equations of motion in Section 2. The emitted vortices can be tracked numerically along with the motion of the cylinder and rivulet. For discs with a circular boundary in such 2-D air flow, complex variable methods exist for the construction of analytic expressions for the fluid velocity field and hence instantaneous integrated dynamic forces on the disc. This approach was used by

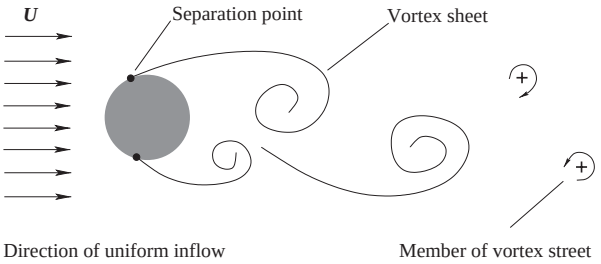

Fig. 16. A sketch of vorticity concentration in the vicinity of a circular disc. The curves of vorticity in 2-D are represented by a sequence of point vortices in 2-D with a re-discretization mechanism. Vorticity streams away from the dynamic separation points on the disc and forms the extended loci attached to its surface. These separate at regular intervals to form detached extended loci where the vorticity is concentrated. A dynamic algorithm determines when to separate such vorticity loci from the disc. When an attached locus is cut the current detached locus is replaced by a coalesced vortex structure, so that there is only one extended detached locus at any instant. The coalesced vortices form a regular street behind the disc. The arrows indicate the direction of the 2-D flow lines induced by the coalesced vortices.

Sarpkaya [28] in a series of investigations of flow around *fixed circular* cylinders and the results compared favourably with experiments in sub-critical domains of flow. A number of the algorithms employed by Sarpkaya have been modified and similar techniques used in Refs. [28–30] to discuss the fluid–structure interaction on *moving* cylinders. Such methods permit one to employ complex mappings to construct analogous expressions appropriate to moving discs with *non-circular* boundaries. A fuller account of such techniques can be found in Refs. [27,30].

As has been argued above the torsional stiffness of the stay cable ensures that one may neglect any rotational motion of the disc about an axis through its centroid. Thus one needs to estimate the 2-D aerodynamic forces at each instant on an arbitrarily translating circular disc with a small protuberance (the rivulet) in 2-D. The forces (torques) contain a component proportional to the acceleration (angular acceleration) of the system and a remainder. Since the density of air is small the former simply adds a small effective mass (rotary inertia) to the mass (rotary inertia) of the system and is of no consequence. Both components can be calculated from the vortex induced forces and torques on a circular disc by effecting the complex transformation below that maps a circle to a particular closed curve that simulates the cross-section of a cylinder with an attached rivulet.

To describe this map let the complex variable $z = x + \mathrm{i}y$ describe points $\{x, y\}$ in the plane in which the *circle* resides.

If

$$\hat{z} = f(z) = z + \frac{a h_r R^2 \mathrm{e}^{2\mathrm{i}(\pi-\varphi)}}{z - bR\mathrm{e}^{\mathrm{i}(\pi-\varphi)}}, \tag{41}$$

then the circle at C, (i.e., $|z| = R$), maps into the contour $f(C)$ illustrated in Fig. 17 with $\varphi = \pi/4$ and $h = h_r R$ with $h_r = 0.1$. This contour will be taken to model the cross-section of the cable with attached rivulet. Thus φ locates the direction of the centroid of the rivulet of height $h = h_r R$ and the dimensionless parameters a, b are chosen to be $a = 0.25$ and $b = 0.75$.

In Fig. 17 the pole of $f(z)$ and zeros of $\mathrm{d}f(z)/\mathrm{d}z$ are marked and are inside the contour for the parameters specified. This ensures that expressions involving $f(z)$ and $\mathrm{d}f(z)/\mathrm{d}z$ on the contour will be regular.

In the plane in which C resides denote the relative incident wind velocity vector (with respect to translational motion of the disc) by the complex number $\mathscr{U}$. The total relative air velocity outside the circle C is represented by the instantaneous complex (conjugate) velocity $\bar{\mathscr{V}}(z)$. The corresponding complex velocity outside $f(C)$ is $\bar{\mathscr{V}}(f^{-1}(\hat{z}))\ \mathrm{d}f^{-1}(\hat{z})/\mathrm{d}\hat{z}$. The field $\bar{\mathscr{V}}$ is constructed from $\mathscr{U}$ and the flow due to a number of point vortices at (complex) instantaneous positions z_{0j} each with an instantaneous vortex strength Γ_j (which is real):

$$\bar{\mathscr{V}}(z) = \bar{\mathscr{U}} - \mathscr{U}\frac{R^2}{z^2} + \bar{\mathscr{V}}_v(z), \tag{42}$$

where the total flow due to a finite number of point vortices is described by the complex velocity:

$$\bar{\mathscr{V}}_v(z) = \sum_j \frac{\Gamma_j}{2\pi \mathrm{i}}\left(\frac{1}{z - z_{0j}} - \frac{1}{z - R^2/\bar{z}_{0j}}\right). \tag{43}$$

The number of terms in the above sum is dynamical and determined by conditions at the complex separation points $\{\zeta_+, \zeta_-\}$ on the disc perimeter where the subscript indicates the sign of vorticity emanating from that point. The domain of $\zeta_+(\zeta_-)$ is taken to be the lower (upper) part of the circle C with diameter in the wind direction $\mathscr{U}$. Each vortex is born at either $z = \zeta_+$ or $z = \zeta_-$ with instantaneous strength

$$\Gamma_\pm = \pm\tfrac{1}{2}|\bar{\mathscr{V}}(\zeta_\pm)|^2 \Delta T \tag{44}$$

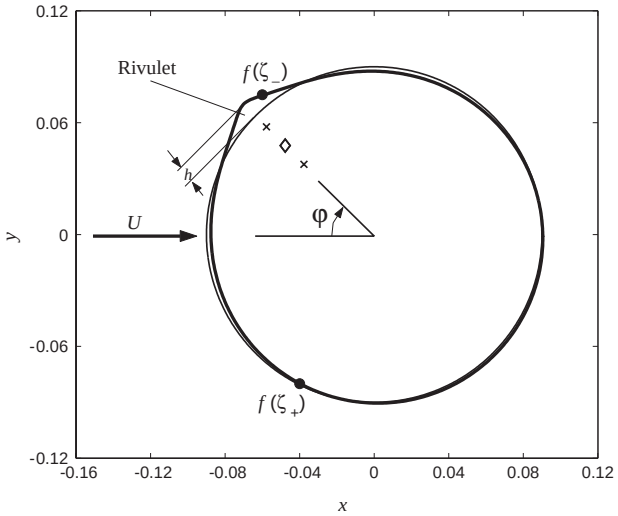

Fig. 17. The complex function f with $\varphi = \pi/4$ and $h_r = 0.1$ maps a circle of radius R into the indicated contour. The points marked $\times$ and $\diamond$ denote the zeroes of $\mathrm{d}f(z)/\mathrm{d}z$ and the pole of $f(z)$, respectively. New vortices are born at the separation points $\{\zeta_+, \zeta_-\}$ at each time step.

depending on its birthplace (see Fig. 17). ΔT is the time step used to evolve the vortices in a numerical simulation of (45), which is chosen to be $\Delta T = 0.2R/|\mathbf{U}|$ i.e. one-tenth of the Strouhal period. For simplicity the vortices in the C plane are evolved according to

$$\frac{\mathrm{d}\bar{z}_{0j}}{\mathrm{d}T} = \lim_{z \to z_{0j}} \left(\bar{\mathscr{V}}(z) - \frac{\Gamma_j}{2\pi \mathrm{i}} \frac{1}{z - z_{0j}} \right). \tag{45}$$

Strictly speaking the pole subtraction in (45) should occur in the $f(C)$ plane, leading to Routh's formula for the vortex velocity on the C plane (see for example Ref. [26]). However, it is expected that the corrections to (45) will be minor given the details of f and the distance of the majority of the vortices from the rivulet. A similar comment should be made about using the velocity in the C plane rather than that in the $f(C)$ plane to calculate the nascent vortex strengths in (44). The hypothesis is that by far the most significant consequence of the presence of the rivulet, in comparison with the situation involving just a circular disc, is the modification of the location of the upper separation point. Corrections to the vortex strengths and velocities (in the C plane) stemming directly from f will be ignored. This point will be further discussed shortly. On examining (42) and (43) it is seen that $\mathscr{U}$ is also the incident wind complex velocity in the $f(C)$ plane because $\hat{z} = f(z) \sim z$ for $|z| \gg R$.

Once the acceleration dependent contribution to the time dependent force has been removed the lift and drag forces on the closed (moving) contour $f(C)$ can be extracted from the complex force $\mathscr{F}$:

$$\bar{\mathscr{F}} = \rho_a \int_C \frac{\mathrm{i}\bar{\mathscr{V}}^2}{2f'} \mathrm{d}\, z - \rho_a \frac{\mathrm{d}}{\mathrm{d}T} \int_C \mathrm{i}\bar{f} \mathscr{V}_v \, \mathrm{d}\bar{z}.$$

Similarly, the torque on the body bounded by $f(C)$ through an axis close to its area centroid is

$$\mathbf{k} \cdot \mathbf{M}^{Tot} = -\rho_a \mathscr{R} \left(\int_C \frac{1}{2} \frac{f}{f'} \bar{\mathscr{V}}^2 \mathrm{d}z \right) + \rho_a \frac{\mathrm{d}}{\mathrm{d}T} \int_C \tfrac{1}{2} f \bar{f} \bar{\mathscr{V}}_v \, \mathrm{d}z.$$

The first term on the right is denoted $-M_1$ and the second M_2. It can be seen that in the simulations as shown in Fig. 18, the first term is the dominant one.

Since the torque on a non-rotating rigid *circular* disc in 2-D potential flow is zero and the disc perimeter is close to a circle, it is expected that this formula will give a reasonable approximation to the instantaneous aerodynamic torque $\mathbf{k} \cdot \mathbf{m}_p$ on the rivulet.

To implement these ideas it is necessary to model the behaviour of boundary layer separation, i.e., $\{\zeta_+, \zeta_-\}$ is needed at each time step. On smooth blunt nosed objects, such as the leading edge of a wing, Thwaites' method [31] offers an economical model to locate boundary layer separation. It is also effective on the boundary of a mobile circular cylinder provided the separation points do not come too close. However, it is not expected that the method will be suitable in the vicinity of a rivulet. In 2-D a disc is adopted as before with a single rivulet located by the dynamic clockwise angle $\varphi < \pi$ measured from the wind inflow direction. Since the rivulet is not expected to migrate too far from its initial position due to aerodynamic pressure forces a model is adopted in which vortex separation occurs in the lower portion of the disc according to Thwaites' method applied in the C plane. For separation on the remaining portion of the boundary a simple heuristic is

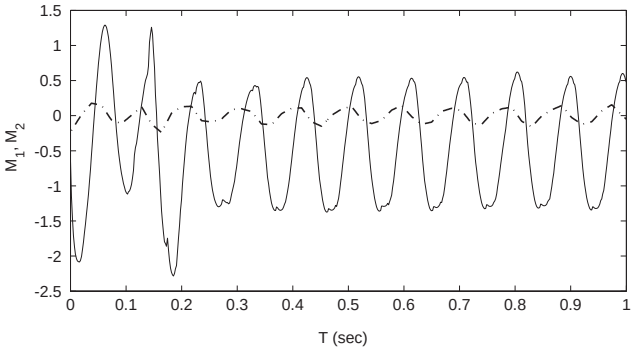

Fig. 18. The time history for the components of the torque on a fixed cylinder with a fixed rivulet at $\varphi = 40^\circ$ and $h_r = 0.2$; —M_1 and $-\cdot-$ M_2.

adopted. For some constant φ^* the second (upper) dynamic separation point is taken to occur at

$$\zeta_- = \begin{cases} \zeta_0 & \text{if } \zeta_0 < \zeta_T, \\ \zeta_T & \text{if } \zeta_0 \geqslant \zeta_T, \end{cases} \tag{46}$$

where

$$\zeta_0 = \tfrac{1}{4}\pi + |\varphi^* - \varphi| \tag{47}$$

and ζ_T is the upper separation point determined by Thwaites' method obtained by *ignoring* the rivulet i.e., again applied in the upper C plane (see Fig. 19). The motivation for (46) is the expectation that the rivulet will be flattened due to the impinging wind, and so have a diminished effect on separation, when it is near to $\varphi = 0$. This heuristic also attempts to recognise that Thwaites' method should be modified when it predicts vortex separation in the vicinity of the rivulet.

The value of φ^* is determined to be $35\pi/180$ rad by numerical experiment to give as close a fit as possible to the measured averaged aerodynamic forces on a fixed cylinder with a fixed rivulet with angle of attack location $\alpha = \varphi$ (see Fig. 3). In Figs. 20–22 a sample of torque histories, lift, drag and torque coefficients for fixed discs with fixed rivulet at $\varphi = 40^\circ, 50^\circ$ and 60° are displayed for such a φ^*. Although the fit involves time averages the associated time histories are not sensitive to this value $\pm 5^\circ$.

For φ in the range from 20° to 100° such curves can be averaged over a given period of time T and the results compared with the wind tunnel date typically displayed in Fig. 3. The smoothed results for the averaged lift, drag and torque coefficients over $T \simeq 1$ second are presented as a function of φ between 20° and 70°. Reasonable comparison with the wind tunnel data is found in this domain as shown in Fig. 23 and provides confidence in the aerodynamic modelling for the *moving* disc and rivulet.

Displacement time histories for the fully coupled non-linear system in which the aerodynamic forces induce motion of the cable with moving rivulets are shown in Fig. 24. The corresponding dynamical drag, lift and torque are depicted in Fig. 25.

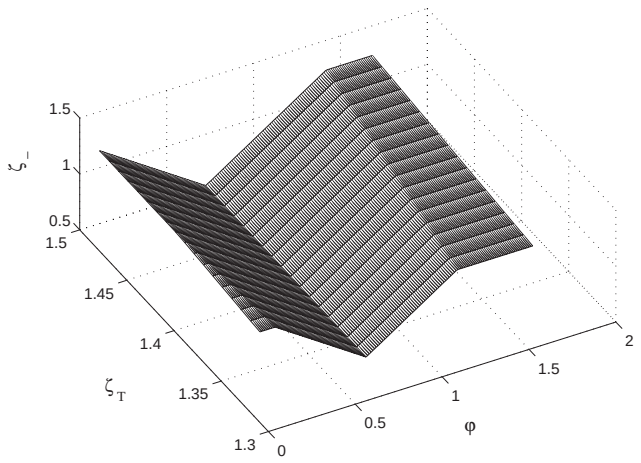

Fig. 19. The figure shows how ζ_- behaves as a function of ζ_T (the separation angle determined by Thwaites' method without the rivulet) and the rivulet location φ.

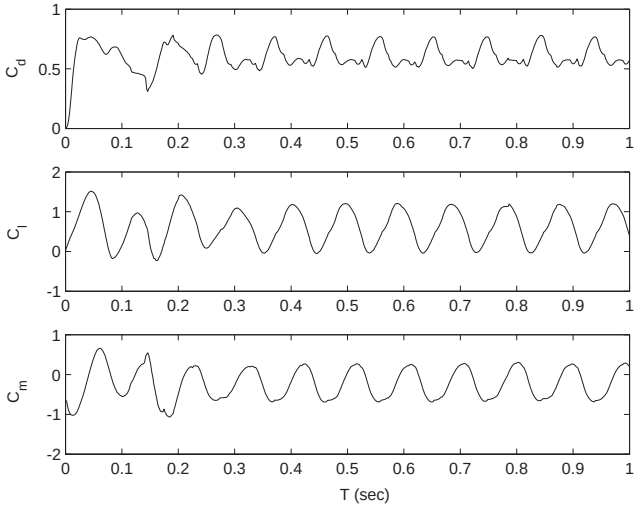

Fig. 20. The drag, lift and torque time histories for a fixed cylinder and a fixed rivulet with $\varphi = 40^\circ$ and $h_r = 0.2$.

5. Conclusions

A system of equations of motion has been analyzed in order to explore the motion of a single straight stay cable in a light wind-rain environment. In addition to gravity the forces on the cable have been modelled in terms of an aerodynamic interaction with an asymmetric 2-D cross-section. This asymmetry is a result of the formation on the cable of a rivulet that may move relative to it. The basic equations of motion of necessity involve a coupling to a wind velocity field and adhesive

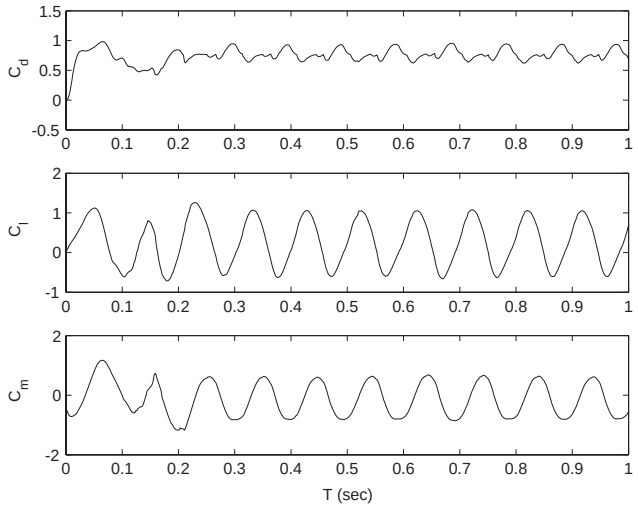

Fig. 21. The drag, lift and torque time histories for a fixed cylinder and a fixed rivulet with $\varphi = 50^\circ$ and $h_r = 0.2$.

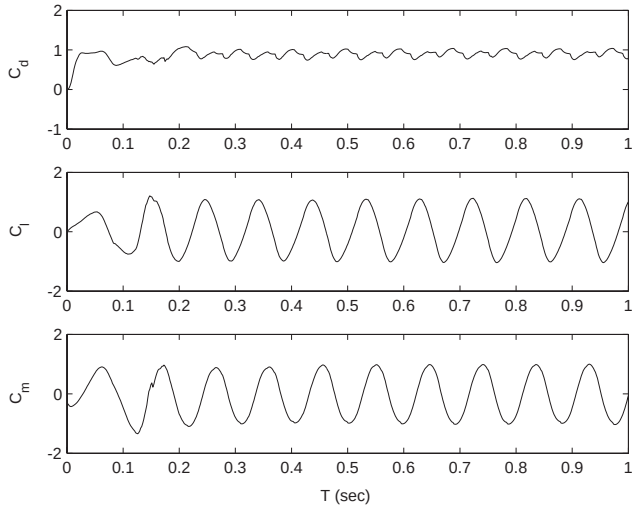

Fig. 22. The drag, lift and torque time histories for a fixed cylinder and a fixed rivulet with $\varphi = 60^\circ$ and $h_r = 0.2$.

forces that bind the rivulet to the surface of the cable. In the first approach a single (upper) rivulet is considered and the equations of motion simplified using time-averaged wind-tunnel data and a parameter R_c. In this approximation a linearized stability analysis has been performed and the dependence of the vibration spectra on R_c and the ambient wind speed explored for various values of the mechanical damping. The eigen-modes contain motions which involve an oscillatory rivulet on a laterally vibrating cable. For certain values of the parameters in the model such motions

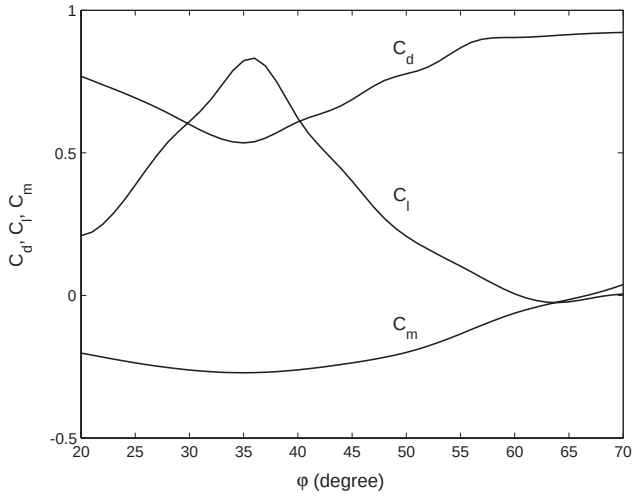

Fig. 23. The time averaged drag, lift and torque coefficients versus the fixed rivulet location φ for a fixed cylinder with $h_r = 0.2$.

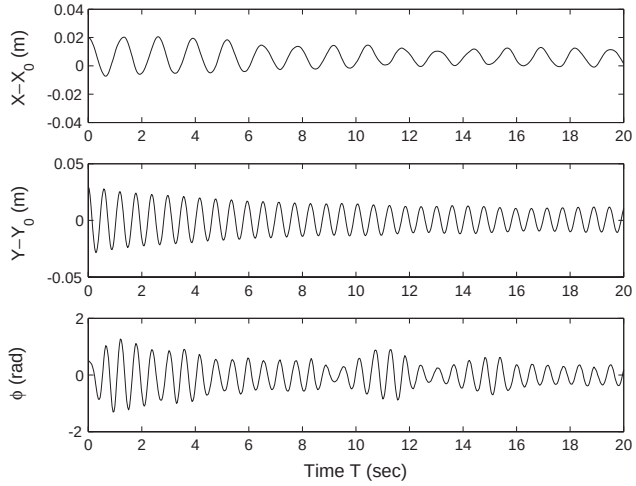

Fig. 24. Displacement time histories for wind speed $U = 10.5$ m/s with initial displacements $X(0) - X_0 = 0.02$, $Y(0) - Y_0 = 0.03$, $\phi(0) = 0.5$ rad and $(\mathrm{d}X/\mathrm{d}T)(0) = (\mathrm{d}Y/\mathrm{d}T)(0) = (\mathrm{d}\phi/\mathrm{d}T)(0) = 0$, $c_x = 4.80$ N s/m^2, $c_y = 4.80\gamma$ N s/m^2, $c_\phi = 0.05$ N s/m. These results arise from the fully coupled non-linear system in which the aerodynamic forces induce motion of the cable with moving rivulets.

become unstable in the linear approximation. To go beyond this approximation an alternative approximation has been considered that does not rely on time-averaged wind-tunnel data and the dependence of the predictions on the parameter R_c. In this approximation two boundary layer separation algorithms were used to simulate the fluid–structure interaction. This in turn was based on a simple boundary layer separation heuristic in which air vorticity in the vicinity of the boundary was concentrated into point vortices that were periodically shed from the cable surface.

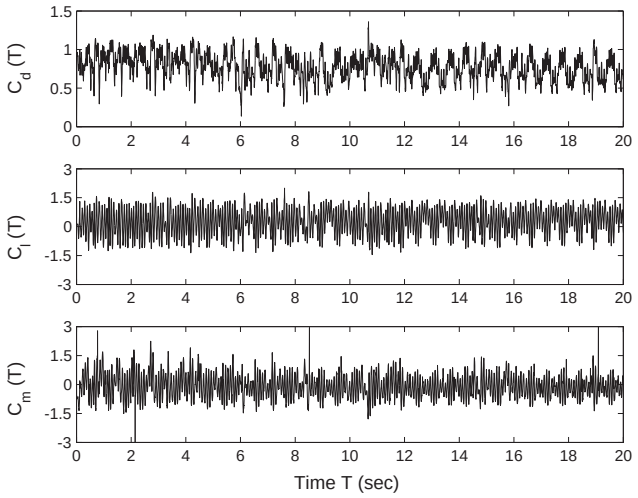

Fig. 25. Dynamical drag, lift and torque for wind speed $U = 10.5$ m/s with initial displacements $X(0) - X_0 = 0.02$, $Y(0) - Y_0 = 0.03$, $\phi(0) = 0.5$ rad and $(\mathrm{d}X/\mathrm{d}T)(0) = (\mathrm{d}Y/\mathrm{d}T)(0) = (\mathrm{d}\phi/\mathrm{d}T)(0) = 0$, $c_x = 4.80$ N s/m^2, $c_y = 4.80\gamma$ N s/m^2, $c_\phi = 0.05$ N s/m. These results arise from the fully coupled non-linear system in which the aerodynamic forces induce motion of the cable with moving rivulets.

The lower moving boundary separation point ζ_+ was determined by Thwaites' method. The moving upper boundary-layer separation point ζ_- was determined both by Thwaites' method and a criterion designed to accommodate the presence of the rivulet. The criterion was expressed in terms of a parameter φ^* which was determined to fit the measured average aerodynamic forces on a fixed cylinder with a fixed rivulet. A sequence of time histories of the resulting non-linear system has been presented and may be compared with results obtained in the linear model.

One significant result that may be inferred from the results of the second approach to the non-linear model is the manner in which it matches well to the measured time averaged values of the drag, lift and torque coefficients for a fixed rivulet on a fixed cylinder using the single parameter φ^* and reasonable damping parameters. This gives some confidence in the dynamical results that follow from this choice of φ^*.

Ultimately, without recourse to detailed fluid dynamical modelling, a commitment to some level of heuristics is inevitable in a system of the type considered here. The two approaches studied above attempt in a simple way to capture some of the physical essentials inherent in the relevant fluid–structure interaction with as few adjustable parameters as possible. The first has the virtue that it employs measured data (that can accommodate different cable surface characteristics) albeit in an average manner and gives rise to a linear eigenvalue problem. The second approach, while more prescriptive, attempts to capture a particular aerodynamic mechanism that permits one to analyze the subtle non-linearities inherent in the equations of motion. The fact that these two approaches produce results with a common overlap is one of the main results of this investigation. The second approach yields a rich dynamic structure and the immediate potential to go beyond the straight cable configuration considered here. It also sheds light on the results of a number of earlier investigations that are limits of the first approach. Both yield results that we feel contribute to a deeper understanding of light rain-wind induced vibrations of slender cables.

Acknowledgements

The authors are most grateful to EPSRC, the TCS, the Royal Academy of Engineering and the staff at Orcina Ltd., Ulverston, for financial support in this investigation and for early discussions with Dr. C Toomer.

References

[1] Y. Hikami, N. Shiraishi, Rain-wind induced vibration of cables in cable stayed bridges, *Journal of Wind Engineering and Industrial Aerodynamics* 29 (1988) 409–418.
[2] R.W. Poston, Cable-stay conundrum, *Civil Engineering* 68 (1998) 58–61.
[3] J.H.G. Macdonald, E.L. Dagless, B.T. Thomas, C.A. Taylor, Dynamic measurements of the Second Severn Crossing, *Proceedings of the Institution of Civil Engineers—Transport* 123 (1997) 241–248.
[4] J.A. Main, N.P. Jones, Full-scale measurements of stay cable vibration, in: A. Larsen, G.L. Larose, F.M. Livesey (Eds.), *Wind Engineering into the 21st Century*, Balkema, Rotterdam, 1997, pp. 963–970.
[5] H. Yamaguchi, Analytical study on growth mechanism of rain vibration of cables, *Journal of Wind Engineering and Industrial Aerodynamics* 33 (1990) 73–80.
[6] M. Matsumoto, N. Shirashi, H. Shirato, Rain-wind induced vibration of cables of cable-stayed bridges, *Journal of Wind Engineering and Industrial Aerodynamics* 41–44 (1992) 2011–2022.
[7] A. Bosdogianni, D. Olivari, Wind- and rain-induced oscillations of cables of stayed bridges, *Journal of Wind Engineering and Industrial Aerodynamics* 64 (1996) 171–185.
[8] C. Versiebe, Exciting mechanisms of rain-wind-induced vibrations, *Structural Engineering International* 8 (1998) 112–117.
[9] M. Matsumoto, T. Yagi, Y. Shigemura, D. Tsushima, Vortex-induced cable vibration of cable-stayed bridges at high reduced wind velocity, *Journal of Wind Engineering and Industrial Aerodynamics* 89 (2001) 633–647.
[10] Y.L Xu, L.Y. Wang, Analytical study of wind-rain-induced cable vibration: SDOF model, *Journal of Wind Engineering and Industrial Aerodynamics* 91 (2003) 27–40.
[11] D.Q. Cao, R.W. Tucker, C. Wang, A stochastic approach to cable dynamics with moving rivulets, *Journal of Sound and Vibration* 268 (2003) 291–304.
[12] M. Matsumoto, T. Yagi, M. Goto, S. Sakai, Rain-wind-induced vibration of inclined cables at limited high reduced wind velocity region, *Journal of Wind Engineering and Industrial Aerodynamics* 91 (2003) 1–12.
[13] O. Nigol, P.G. Buchan, Conductor galloping Part 2—torsional mechanism, *IEEE Transactions on Power Apparatus and Systems* PAS-100 (1981) 708–720.
[14] J.P. Den Hartog, Transmission line vibration due to sleet, *American Institute of Aeronautics and Astronautics Transactions* 51 (1932) 1074–1076.
[15] E. Simiu, R.H. Scanlan, *Wind Effects on Structures*, Wiley, New York, 1996.
[16] R.D. Blevins, W.D. Iwan, The galloping response of a two-degree-of-freedom system, *Transactions of the American Society of Mechanical Engineers, Journal of Applied Mechanics* 41 (1974) 1113–1118.
[17] P. Yu, A.H. Shah, N. Popplewell, Inertially coupled galloping of iced conductors, *Transactions of the American Society of Mechanical Engineers, Journal of Applied Mechanics* 59 (1992) 140–145.
[18] K.F. Jones, Coupled vertical and horizontal galloping, *American Society of Civil Engineers, Journal of Engineering Mechanics* 118 (1992) 92–107.
[19] A. Luongo, G. Piccardo, Non-linear galloping of sagged cables in 1: 2 internal resonance, *Journal of Sound and Vibration* 214 (1998) 915–940.
[20] P. Yu, Y.M. Desai, A.H. Shah, N. Popplewell, Three-degree-of-freedom model for galloping, part I: formulation, *American Society of Civil Engineers, Journal of Engineering Mechanics* 119 (1993) 2404–2425.
[21] P. Yu, Y.M. Desai, N. Popplewell, A.H. Shah, Three-degree-of-freedom model for galloping, part II: solutions, *American Society of Civil Engineers, Journal of Engineering Mechanics* 119 (1993) 2426–2448.
[22] D.Q. Cao, R.W. Tucker, C. Wang, Aeroelastic stability of a Cosserat stay cable, *Proceedings of the Fourth International Symposium on Cable Dynamics*, Montreal, Canada, 2001, pp. 369–376.

[23] R.D. Blevins, *Flow-Induced Vibration*, Van Nostrand Reinhold Company, New York, 1977.
[24] R.K. Miller, A.N. Michel, *Ordinary Differential Equations*, Academic Press, London, 1982.
[25] H.M. Irvine, *Cable Structures*, The MIT Press, Cambridge, 1981.
[26] T. Sarpkaya, Computational methods with vortices: the 1988 Freeman Scholar lecture, *Journal of Fluids Engineering* 111 (1989) 5–52.
[27] D.J. Acheson, *Elementary Fluid Dynamics*, Oxford University Press, Oxford, 1990.
[28] T. Sarpkaya, Vortex-induced oscillations, *Transactions of the American Society of Mechanical Engineers, Journal of Applied Mechanics* 46 (1979) 241–258.
[29] T. Sarpkaya, R.L. Schoaff, Inviscid model of two-dimensional vortex shedding by a circular cylinder, *American Institute of Aeronautics and Astronautics Journal* 17 (1979) 1193–1200.
[30] D. Burton, D. Hartley, R.W. Tucker, Vortex-induced fluid forces on accelerating rigid boundaries in 2 dimensions. *Proceedings Fifth International Seminar on Geometry, Continua & Microstructure*, Sinaia, Romania, Editura Academiei Romane, 2001.
[31] A.D. Young, *Boundary Layers*, BSP Professional Books, Oxford, 1989.